DOI: 10.13009/EUCASS2017-247

DOI: 247

Large-eddy simulation of multi-element LOx/H_2 combustion at transcritical conditions

Julian Zips[*], *Hagen Müller*[†] *and Michael Pfitzner*
Thermodynamics Institute, Bundeswehr University Munich
Werner-Heisenberg-Weg 39, 85577 Neubiberg, Germany

Justin Hardi and Michael Oschwald
German Aerospace Center (DLR), Institute of Space Propulsion Hardthausen
Langer Grund, 74239 Hardthausen, Germany

Abstract

This study presents a numerical method for the efficient large-eddy simulation (LES) of non-premixed combustion at supercritical pressures. A flamelet-based approach is extended to incorporate real-gas thermodynamics at moderate computational cost. Real-gas effects are taken into account using the cubic Peng-Robinson equation of state. The resulting model with its assumptions is assessed and the respective errors are quantified. Its computational cost are comparable to ideal gas simulations. The method is consequently applied to the multi-element LOx/H_2 rocket combustor BKH operated at DLR Lampoldshausen. A supercritical operating point with injection conditions typical for liquid rocket engines is used as reference case. Both instantaneous and time-averaged LES results are compared to experimental shadowgraph and OH* emission images.

1. Introduction

The operating conditions of liquid propellant rocket engines (LRE) are often characterized by high chamber pressures that can easily exceed the critical pressure of the propellants. Additionally, it is common to inject the oxidator at cryogenic temperature, which causes real-gas thermodynamic effects. Fluid properties, i.e., density, heat capacity or transport properties are then non-linear functions of temperature and pressure, which affects injection, mixing and combustion. As the pressure becomes sufficiently high, the mixing process resembles dense gas mixing as the surface tension between liquid and gas vanishes which was shown experimentally by Mayer *et al.*[14,15] The mixing layer nevertheless exhibits significant variations of the fluid properties within a tiny region as the fluid changes from a liquid-like to a gas-like state.[30] Similar conditions may arise in other high-pressure combustion devices such as modern gas turbines or Diesel engines. In order to investigate the nature of such flows at rocket-like conditions, numerous experiments have been conducted and comprehensive overviews are amongst others given by Habiballah *et al.*,[22] Oschwald *et al.*[22] or Chehroudi.[1] Parallel to the experimental progress, numerical tools to simulate near-critical mixing and combustion have been developed. Amongst others, Oefelein and Yang,[20] Zong *et al.*[34] and Oefelein[21] discuss the challenges and requirements of time-resolved flow field prediction of cryogenic mixing at supercritical pressures. They indicate that the incorporation of a suitable equation of state and thermodynamic relations is crucial for flow field predictions under these conditions. The computation of real-gas thermodynamics is computationally expensive and in the context of reacting flows, additional transport equations and the solution of chemical source terms further increase the computational cost. Different combustion models have been used to simulate cryogenic jet flames using LES, e.g., an infinitely fast chemistry approach by Schmitt *et al.*[28] or a reduced global reactions mechanism by Guézennec *et al.*[5] Recently, studies with multi-element injector configurations focused on combustion instabilities have been published by Hakim *et al.*,[6] who used an infinitely fast chemistry model and Urbano *et al.*[32] who employed an extended equilibrium method. However, LES incorporating real-gas thermodynamics and combustion is still computationally demanding which limits its applicability. But, due to the method's promising capability to provide further understanding of the involved physical phenomena, it is valuable to further develop the numerical tools and reduce the computational cost of real-gas thermodynamics in combination with chemical reactions for the simulation of trans-critical flames. In the present paper we

[*]julian.zips@unibw.de
[†]Now at: MTU Aero Engines AG, Dachauer Str. 665, 80995 München. hagen.mueller@mtu.de

DOI: 10.13009/EUCASS2017-247

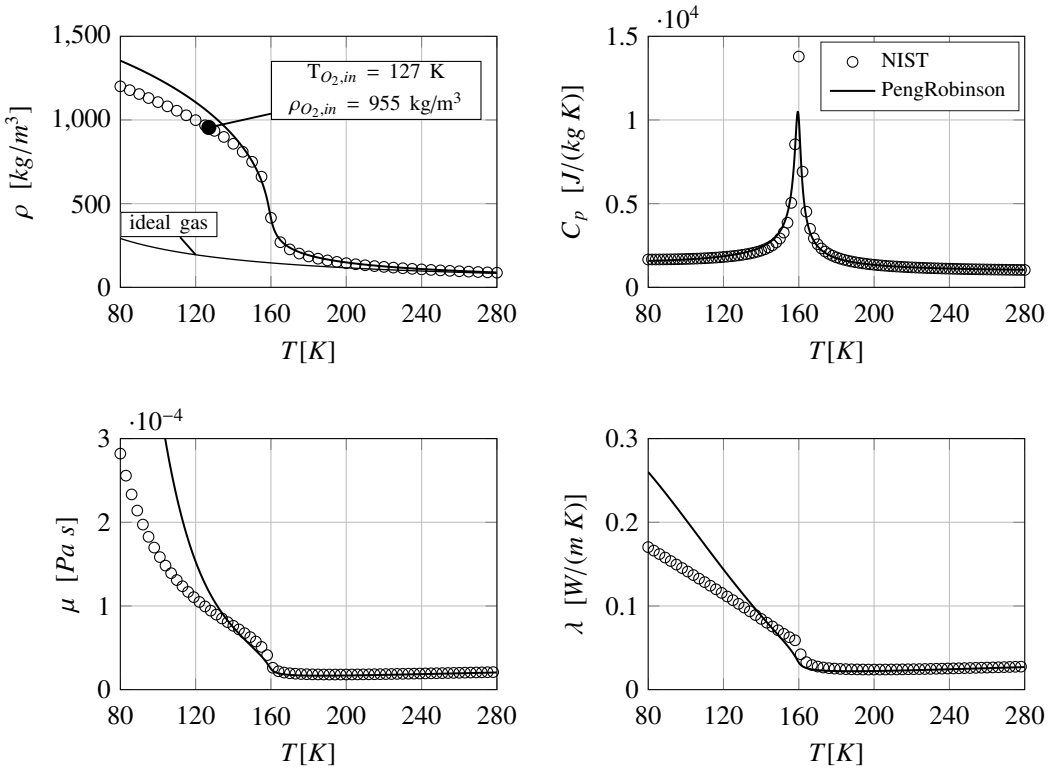

Figure 1: Real-gas thermodynamic properties for O_2 at $p = 60.7$ bar. Reference data taken from the NIST webbook.[13]

propose a method with slightly reduced fidelity but significantly reduced computational cost. The formulation is based on a tabulated chemistry approach and accounts for real-gas thermodynamics using a cubic equation of state. In Sec. 2, the underlying assumptions are discussed and the introduced inaccuracies are quantified. Consequently, the model is applied to perform LES of a multi-element LOx/GH$_2$ flame at the operating conditions investigated experimentally by Hardi *et al.*[7,8] at the DLR in Lampoldshausen.

2. Numerical Method

2.1 Thermodynamics

The Peng-Robinson equation of state[23]

$$p = \frac{RT}{v-b} - \frac{a}{v^2 + 2vb - b^2} \tag{1}$$

is used to relate the thermodynamic quantities. Here, p is the pressure, R is the gas constant and v is the molar volume of the mixture. The parameters a and b account for intermolecular forces and the reduction of free volume, respectively. a and b are calculated using the mixing rules of Harstad *et al.*[9] as functions of the critical pressure and temperature. The Peng-Robinson equation of state yields accurate results around the critical temperature and for higher values. However, deviations from the NIST reference data[13] can be observed at lower temperatures, especially for density, which is shown in Fig. 1 for oxygen at $p = 60.7$ bar corresponding to the test case configuration of Hardi *et al.*[8] Since the oxygen injection temperature in the test case is $T_{inj,O_2} = 127$ K, which is relatively close to the critical temperature $T_{cr,O_2} = 154.58$ K, we accept the introduced error and employ the unmodified Peng-Robinson equation of state. At injection conditions, the computed density is $\rho_{inj,O_2} = 1045.35$ kg/m^3 compared to the reference value of $\rho_{inj,O_2,NIST} = 955$ kg/m^3. The departure function formalism is applied to calculate the caloric properties.[25] Therefore, the respective quantity is decomposed into an ideal part, which is evaluated at low reference pressure with the NASA polynomials and a departure contribution, which is pressure dependent and calculated using Eq. 1. Fig. 1 additionally shows the transport properties, i.e., molecular viscosity and thermal conductivity, which are computed using the empirical correlations of Chung *et al.*[2] and agree well to the NIST reference data within the temperature range of interest.

DOI: 10.13009/EUCASS2017-247

Table 1: Critical properties of oxygen and hydrogen.

	p_c [bar]	T_c [K]
O_2	50.430	154.581
H_2	12.964	33.145

2.2 Combustion Model

The present section briefly discusses the flame structure of laminar LOx/H_2 counterflow diffusion flames in order to motivate the choice of combustion model for the subsequent LES of the DLR model combustor. Therefore, the flamelet equations[24] have been implemented earlier to OpenFOAM allowing for consistent treatment of the thermodynamics. The Lewis number is assumed to be unity and Soret and Dufour effects are neglected. The species source terms are computed using the H_2/O_2 reactions mechanism of O'Connaire *et al.*[19] which includes eight species (H, H_2, O, O_2, OH, H_2O, HO_2, H_2O_2) and 19 elementary chemical reactions. The equations are solved in mixture fraction space using 530 grid points with increased mesh density in regions of strong gradients. Several laminar diffusion flames are computed at $p_{op} = 60.7$ bar with $T_{O_2} = 127$ K and $T_{H_2} = 279$ K as boundary conditions according to the operating conditions of Hardi *et al.*[7,8] An extensive analysis of LOx/H_2 diffusion flames at relevant pressures can be found in Ribert *et al.*[26] and Lacaze and Oefelein.[12] Fig. 2 shows the typical flame structure at supercritical pressure for a range of scalar dissipation rates χ_{st}. It is observed that the flame is robust to effects of strain up to $\chi_{st} \approx 1 \cdot 10^4$ 1/s. By further increasing χ_{st}, the maximum temperature is monotonically reduced until extinction occurs at values beyond $\chi_{st} \geq 1 \cdot 10^6$ 1/s which is considerably larger than the maximum strain encountered in the LES later on. Selected temperature profiles in mixture fraction space are shown on the right hand side of Fig. 2. The maximum temperature is reached around stoichiometry $f_{st} = 0.11$ and decreases with higher strain rates preserving the over-all shape of the profile. Since the reaction rates scale with the pressure, flames at higher pressure are increasingly robust to strain.[26] The flame thickness is inversely proportional to $\sqrt{p}$, hence the flames are very thin. The following comparison between ideal gas and real-gas thermodynamics is performed using a representative flamelet at low scalar dissipation rate $\chi_{st} \approx 1$.

Fig. 3 shows the profiles of temperature, density and selected species mass fractions in mixture fraction space and the respective relative error between ideal gas and real-gas formulation computed by $\varepsilon_\phi = |\phi_{ideal} - \phi_{real}| / \phi_{real}$. Note that except for the left column, the quantities are shown in logarithmic scale to emphasize the differences in the region, where the solution is affected by real-gas effects. The maximum temperature as well as the over-all shape are almost identical in both cases. However, the logarithmic plot highlights the effect of the transition of the liquid-like to the gas-like state. This pseudo-boiling is not reflected by ideal gas thermodynamics, which leads to lower temperatures for the real-gas flamelet in comparison to the ideal gas solution (c.f. also the peak in heat capacity in Fig. 1). The relative error in temperature accounts for up to 70 % in this region. Regarding the density, one clearly observes the need for an accurate equation of state at cryogenic temperatures to properly capture the injection density. Here, the relative error comes to more than 80 % at the oxidizer inlet and diminishes to negligible values starting from $f \approx 5 \cdot 10^2$. Notably, the deviations are not restricted to regions where the compressibility factor $Z = pv/RT$ is lower than 1 and the equation of state plays a dominant role. Even in regions of $Z \approx 1$, where the cubic equation of state reduces to the ideal gas constitution, the solutions are not identical. This is mostly caused by the difference in enthalpy due to its pressure dependent part, which is not included in the ideal gas simulation, see Fig. 4. The flamelet equations state that a passive scalar such as the enthalpy is a linear function of the mixture fraction and consequently the boundary values at oxidizer and fuel side determine the enthalpy across the flame. The differences at the boundaries are prescribed by the departure function contribution. Comparing the main species reveals that the mixture composition is only weakly affected by the thermodynamics model. Both, the linear and the logarithmic plot do not show notable differences over the whole mixture fraction space. The absolute deltas in O_2, H_2, H_2O and OH mass fraction between ideal gas and real-gas flamelet are below $5 \cdot 10^{-3}$ around stoichiometry. The deviations become smaller towards the fuel side, where only diffusive processes are active. Here, the species mass fraction profiles are linear curves and the error is constant. Note that within the region $Z \leq 1$, where the equation of state is predominant, the mixture mostly consists of oxygen.

From the previously presented results we draw the conclusion, that the incorporation of real-gas thermodynamics is necessary to obtain meaningful results in flame regions with $Z \leq 1$, i.e., to predict the correct density at the boundaries and to reflect the pseudo-boiling process. Additionally, the departure function contribution to the enthalpy should be incorporated to improve the modeling of temperature and density in regions of $Z \approx 1$, where the equation of state reduces to the ideal gas formulation. Keeping in mind that solvers for real-gas counterflow diffusion flames are still not as widespread as their ideal-gas versions and that solving finite rate chemistry together with real-gas thermodynamics is computationally expensive, we propose a method to efficiently incorporate real-gas effects in trans-

DOI: 10.13009/EUCASS2017-247

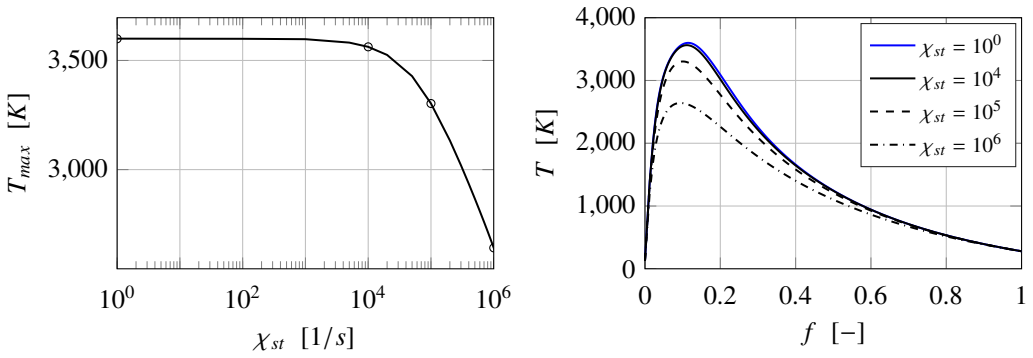

Figure 2: Effect of the strain rate. The dots on the left hand side correspond to the particular solutions shown on the right hand side.

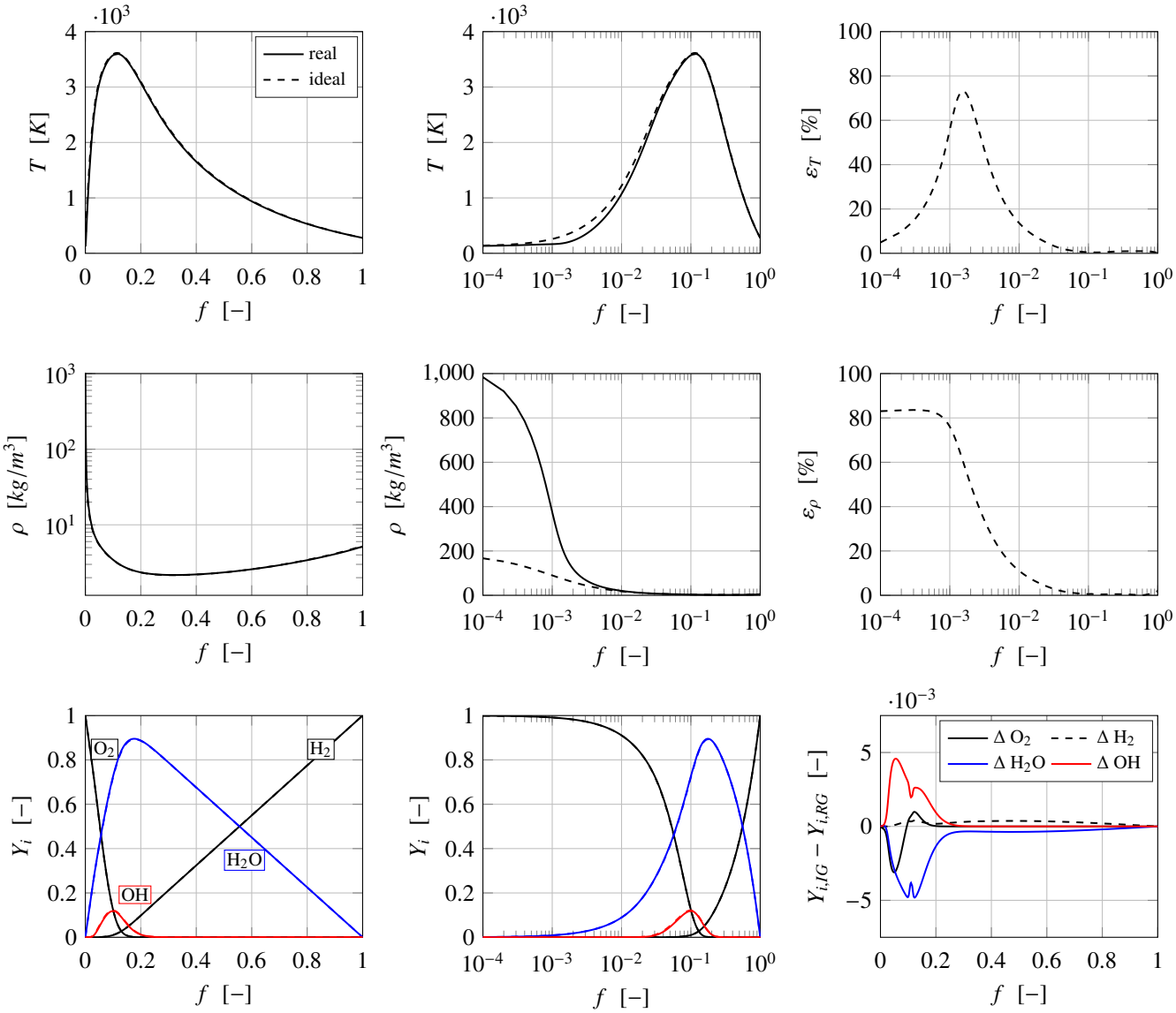

Figure 3: Comparison of flamelet solutions for H_2/O_2 combustion at $x = 60.7$ bar for $\chi_{st} \approx 1$ using real-gas and ideal gas thermodynamics.

DOI: 10.13009/EUCASS2017-247

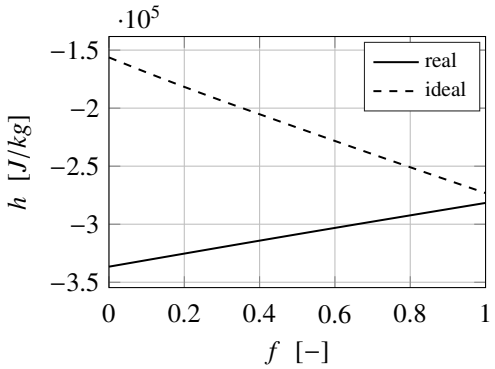

Figure 4: Enthalpy of the one-dimensional counterflow diffusion flame using real-gas and ideal gas thermodynamics.

critical flames in the flamelet regime. The procedure is as follows: We use the result, that the differences in mixture composition are small between real-gas and ideal gas flamelet, c.f. Fig. 3, and generate ideal gas solutions over a range of scalar dissipation rates at the boundary conditions of interest. Then, we make use of the linear shape of the enthalpy and correct the enthalpy values over the whole mixture fraction space for its pressure-dependent part using the departure function formalism and the known boundary conditions. This pressure-dependence of the enthalpy must later on be reflected in the LES to ensure energy conservation. Then, we employ the thermodynamics model described above with the mixture composition from the ideal gas solution and the corrected enthalpy to determine the thermo-chemical state of the mixture at every point of the flamelet. The use of the ideal gas species mass fractions introduces an error, which is expected to be small as shown in Fig. 3. Finally, a Favre presumed probability density function (PDF) approach is applied to calculate the mean values of species mass fractions, temperature, density, compressibility, transport properties and speed of sound, which are required for the CFD code. Here, a β-PDF is used for the mixture fraction and Dirac functions for scalar dissipation rate and pressure. Hence, the thermo-chemical library is stored as $\widetilde{\Phi} = \widetilde{\Phi}(\widetilde{f}, \widetilde{f''^2}, \widetilde{\chi}_{st}, \widetilde{p})$ to be accessed during the LES. In this method, both the detailed finite rate and the real-gas thermodynamics calculations are performed in a pre-processing step and can be done in an arbitrary scripting environment. Hereby, the overall computational cost are significantly reduced to a level comparable with common ideal gas simulations. A more detailed assessment of the model is soon to be published elsewhere. In the LES of the test case of Hardi *et al.*,[7,8] the database is discretized using 1011 points in $\widetilde{f}$ with a clustering around strong gradients, 10 points in $\widetilde{f''^2}$, 6 points in χ_{st} and 29 values of $\widetilde{p}$ around the operating pressure.

2.3 Governing Equations

The theoretical model explained above is embedded in the OpenFOAM LES framework. The filtered governing equations in the LES approach are given in Cartesian coordinates x_i and time t by the conservation of mass

$$\frac{\partial \bar{\rho}}{\partial t} + \frac{\partial}{\partial x_i}\left(\bar{\rho}\tilde{u}_i\right) = 0, \tag{2}$$

where ρ is the density and u_i is the velocity vector. The momentum equations are

$$\frac{\partial}{\partial t}\left(\bar{\rho}\tilde{u}_i\right) + \frac{\partial}{\partial x_j}\left(\bar{\rho}\tilde{u}_i\tilde{u}_j\right) = -\frac{\partial \bar{p}}{\partial x_i} + \frac{\partial}{\partial x_j}\left(2\left(\bar{\mu} + \mu_{sgs}\right)\left(\tilde{S}_{ij} - \frac{1}{3}\tilde{S}_{kk}\delta_{ij}\right)\right), \tag{3}$$

where μ is the molecular viscosity and S_{ij} is the resolved strain tensor

$$\tilde{S}_{ij} = \frac{1}{2}\left(\frac{\partial \tilde{u}_i}{\partial x_j}\frac{\partial \tilde{u}_j}{\partial x_i}\right). \tag{4}$$

The bar denotes the finite-volume filter and the tilde represents Favre-filtering. The Boussinesq assumption has been introduced to write the subgrid stress tensor as

$$\tau_{ij} = \bar{\rho}\left(\widetilde{u_i u_j} - \tilde{u}_i\tilde{u}_j\right) = 2\mu_{sgs}\left(\tilde{S}_{ij} - \frac{1}{3}\tilde{S}_{kk}\delta_{ij}\right) - \frac{2}{3}\bar{\rho}k\delta_{ij}. \tag{5}$$

μ_{sgs} is the eddy viscosity which is determined using the Vreman SGS model.[33] The library of the tabulated combustion model is linked to the flow field using four access parameters. First, the evolution of the mixture fraction f is described

DOI: 10.13009/EUCASS2017-247

by

$$\frac{\partial}{\partial t}\left(\bar{\rho}\tilde{f}\right) + \frac{\partial}{\partial x_j}\left(\bar{\rho}\tilde{u}_j\tilde{f}\right) = \frac{\partial}{\partial x_j}\left(\left(\frac{\bar{\mu}}{Sc} + \frac{\mu_{sgs}}{Sc_t}\right)\frac{\partial\tilde{f}}{\partial x_j}\right). \tag{6}$$

Second, a transport equation is solved for the mixture fraction variance $\widetilde{f''^2}$

$$\frac{\partial}{\partial t}\left(\partial\bar{\rho}\widetilde{f''^2}\right) + \frac{\partial}{\partial x_j}\left(\bar{\rho}\tilde{u}_j\widetilde{f''^2}\right) = \frac{\partial}{\partial x_j}\left(\left(\frac{\bar{\mu}}{Sc} + \frac{\mu_{sgs}}{Sc_t}\right)\frac{\partial\widetilde{f''^2}}{\partial x_j}\right) - 2\bar{\rho}\tilde{\chi} + 2\left(\frac{\bar{\mu}}{Sc} + \frac{\mu_{sgs}}{Sc_t}\right)\left(\frac{\partial\tilde{f}}{\partial x_j}\right)^2. \tag{7}$$

In Eqs. 6 and 7, the standard gradient assumption is employed to model the respective diffusive term. The diffusion coefficient is expressed by dividing the viscosities μ and μ_{sgs} through a molecular and turbulent Schmidt number Sc and Sc_t, respectively. In the present study the parameters are chosen to be constant as $Sc = Sc_t = 1$. The third control variable is the scalar dissipation rate, which is decomposed into resolved part and SGS contribution

$$2\bar{\rho}\tilde{\chi} = 2\frac{\tilde{\mu}}{Sc}\left(\frac{\partial\tilde{f}}{\partial x_j}\right)^2 + C_\chi\frac{\mu_{sgs}}{Sc_t}\frac{\widetilde{f''^2}}{\Delta^2}, \tag{8}$$

where Δ is the filter size and the constant is set to $C_\chi = 2$. To ensure energy conservation, the tabulated state is finally retrieved using the local pressure as the fourth library parameter.

The fully parallelized open-source CFD toolbox OpenFOAM[1] is used for all simulations. The pressure-based solution algorithm for transonic flows employed here represents a compressible version of the PISO method. The code has been extended in order to incorporate the real-gas thermodynamics and the tabulated combustion model discussed in Sec. 2. This numerical framework has been successfully used for the simulation of non-reacting and reacting flows under trans- and supercritical conditions.[16–18] A second-order central differences scheme with van Leer TVD limiter is employed for spatial discretization for all variables. For temporal discretization a first-order implicit Euler scheme is used with a maximum local convective Courant number of $Cn = 0.2$. Additionally, localized artificial dissipation[3] had to be used to avoid unreasonable pressure oscillations in regions of high density gradients. Therefore, an artificial viscosity is computed by

$$\mu^* = C_\mu\,\bar{\rho}\,a_s\,\Delta^2\left|\frac{\partial Z}{\partial x_j}\right| \tag{9}$$

a_s and Δ are the speed of sound and the local filter width, respectively. The constant C_μ is set to 0.08. Here, the local gradient of the compressibility factor ($Z = pv/RT$) is used as a sensor, which becomes zero where real-gas effects are vanishing. The artificial viscosity is then added to the molecular viscosity in the LES. A similar method has been used by Terashima *et al.*[31]

3. Test Case

The described computational model is applied to simulate the flow in the model combustor named BKH which is operated at the DLR Lampoldshausen. It is designed to operate at pressures between 40 and 60 bar and uses LOx/H$_2$ as propellants with injection parameters representative for industrial upper stage LREs. The combustor serves for the investigation of combustion instabilities and can be exposed to acoustic forcing. It provides optical access allowing for high-speed measurements in terms of shadowgraphy and OH* imaging. For detailed description of BKH, experimental methods and results refer to Hardi *et al.*[7,8]

3.1 Experimental Setup

Fig. 5 schematically shows the geometry of the BKH combustion chamber and the dimensions of the optical access, which has a height of 50 mm and a length of 100 mm. In the present study we consider a steady state operating point without acoustic forcing at a nominal combustion chamber pressure of 60.7 bar. Propellants are supplied by five shear-coaxial elements with one central element and four surrounding elements. The LOx pipe diameter is 3.5 mm, the inner and outer H$_2$ annulus diameters are 4.7 mm and 5.8 mm, respectively. Consequently, the post tip width is 0.6 mm. In order to protect the windows from hot gases, a H$_2$ cooling film is injected from slots at the walls on both sides of the injector. Secondary H$_2$ is injected from orifices above and below the primary injector to reduce the thermal loads on the combustor. In the considered operating point, the propellant mass flow rates per element are $\dot{m}_{LOx} = 0.113$ kg/s and $\dot{m}_{H_2} = 0.019$ kg/s. Oxygen is injected at cryogenic temperature of $T_{LOx} = 127$ K while the fuel enters the chamber at

[1] www.openfoam.org

DOI: 10.13009/EUCASS2017-247

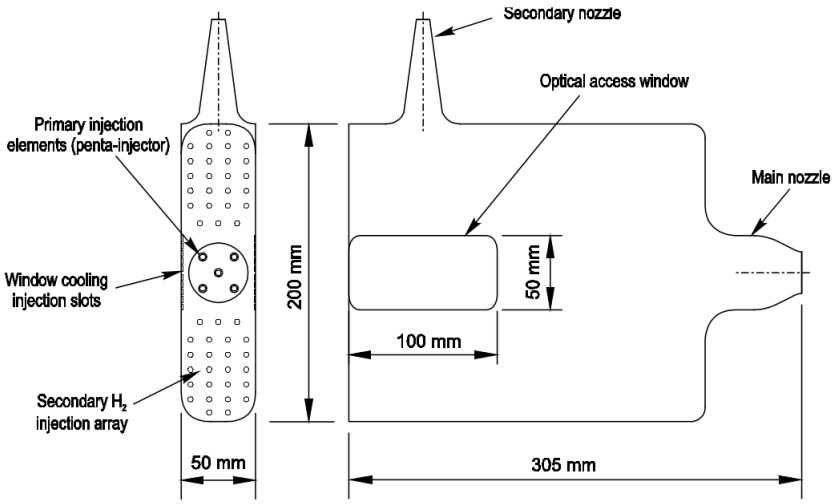

Figure 5: Schematic of the BKH combustor, taken from Hardi *et al.*.

ambient temperature $T_{H_2} = 279$ K. The injection parameters are summarized in Tab. 2, where the density is evaluated using the NIST database.[13] The injection velocity ratio is given by

$$J = \frac{U_{H_2}}{U_{O_2}} = 33.33 \tag{10}$$

and the momentum flux ratio is

$$M = \frac{\rho_{H_2} U_{H_2}^2}{\rho_{O_2} U_{O_2}^2} = 5.92. \tag{11}$$

Table 2: Injection conditions

	ρ_{in} [kg/m^3]	T_{in} [K]	u_{in} [m/s]	$\dot{m}_{in}$ [kg/s]
Per element O_2	955	127	12.3	0.113
Per element H_2	5.08	279	410	0.019
Total secondary H_2	5.09	278	367	0.899
Total window H_2	5.04	281	662	0.260

3.2 Numerical Setup

First, single-element simulations are carried out to investigate meshing requirements, simulation time sequence and inlet boundary conditions at reasonable computational cost. Therefore, one injector element is placed in a cylindrical domain with a diameter of 0.06 m, which ensures sufficient distance between the region of interest and the outer walls. The domain length is set to $x = 0.150$ m, where the last third shows increasing cell sizes and thus serves as sponge layer to minimize interaction with acoustic waves generated at the outlet. Within the single-element simulations the outer walls, the faceplate and the post-tip are considered as adiabatic no-slip walls. The inlet boundary conditions for the propellants are set according to the experiment. The corresponding injection densities evaluated assuming constant chamber pressure $p_c = 60.7$ bar are $\rho_{O_2,in} = 955\,\mathrm{kg\,m^{-3}}$ and $\rho_{H_2,in} = 5.08\,\mathrm{kg\,m^{-3}}$, respectively. The window H_2 cooling film and the secondary H_2 inlets are not considered in the simulation using a single injection element. At the outlet, a constant pressure of 60.7 bar is prescribed. Simulations are carried out for three different numerical grids, see Tab. 3. In a second step, the five injection elements are fully resolved, see Fig. 6. The hydrogen cooling film at the windows is resolved as well although the particular injection slots are simplified to a continuous film applicator. In order to ensure an environment similar to the experiments, the secondary H_2 flow is included and modeled as uniform inlet stream over the faceplate as denoted in Fig. 6. The total computational domain reaches in vertical direction from $y = -80$ mm to $y = 80$ mm, in spanwise direction from $z = -25$ mm to $z = 25$ mm and in axial direction from $x = 0$ mm to $x = 150$ mm. As seen in Fig. 5, the domain does not account for the whole combustion chamber but sufficiently comprises the area

DOI: 10.13009/EUCASS2017-247

Table 3: Mesh characteristics

case	posttip resolution	O_2 resolution	H_2 resolution	axial resolution	total no. cells
BKH-A-SE-01	6	12	6	295	$0.31 \cdot 10^6$
BKH-A-SE-02	12	24	11	590	$2.5 \cdot 10^6$
BKH-A-FI-01	12	24	11	590	$20 \cdot 10^6$

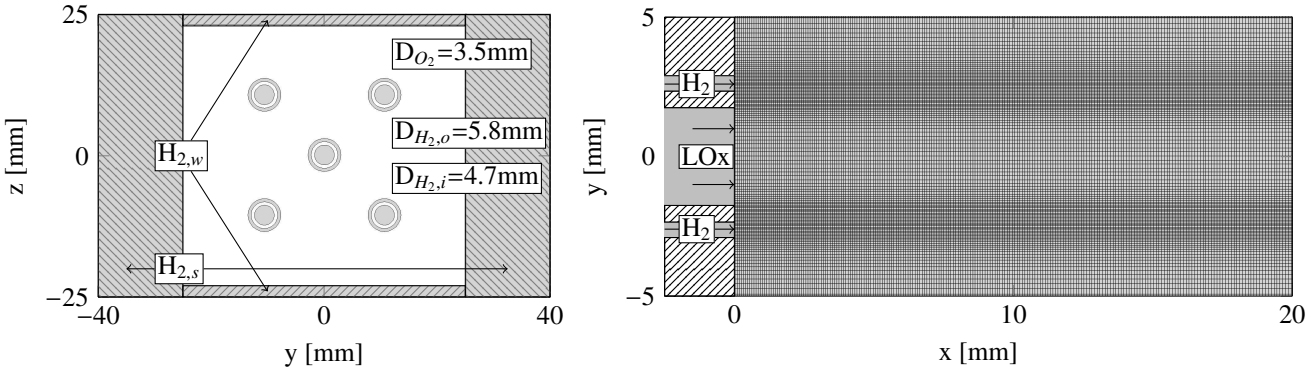

(a) Injector pattern.

(b) Near-injector element grid resolution.

Figure 6: Left: Injector pattern and additional hydrogen injection faces for the five-element configuration. $H_{2,w}$ denotes the inlet slot for the window cooling film, $H_{2,s}$ is the secondary hydrogen injection area. Right: Injector-near detail of the medium mesh.

of interest, as the window in the experiment is in between $y = -25\,\text{mm}$ to $y = 25\,\text{mm}$ and $x = 0\,\text{mm}$ to $x = 100\,\text{mm}$ using the same coordinate system.

4. Results

4.1 Single-Element Simulation

Mesh sensitivity

Two subsequently refined meshes serve to evaluate the influence of grid resolution to the results on th basis of the single-element configuration as listed in Tab. 3. Radial profiles of temperature and its RMS at three axial positions are shown in Fig. 7. Despite the overall agreement of the profiles, it can be observed that the core length is affected by the mesh resolution. Insufficient grid density leads to over-estimated diffusion and thus to sooner jet break-up. This is especially evident at $x = 50\,\text{mm}$, where the mean temperature at the axis is clearly lower on the finer mesh, although its RMS values show less deviations. At this point, at least on further refinement is required to evaluate mesh convergence. A consecutive increase in mesh density by a factor of two in each dimension results in $20 \cdot 10^6$ cells in the single element case. For the cause that the computational grid of the full injector simulation with a mesh density corresponding to the next refinement level yields approximately $160 \cdot 10^6$ cells, the mesh density of the second mesh is used in the present study. This compromise is accepted for now and the investigation of further grid refinement is currently ongoing.

Time averaging sequence

To quantify the simulation time required to wash out the initial flow field and to obtain a statistically converged solution, the flow through time is estimated by the method of Ruiz *et al.*[27] A convective velocity can be estimated by

$$U_{conv} = \frac{U_{O_2} + (\rho_{H_2}/\rho_{O_2})^{1/2}\, U_{H_2}}{1 + (\rho_{H_2}/\rho_{O_2})^{1/2}} = 39.35\,\text{m}\,\text{s}^{-1}, \tag{12}$$

DOI: 10.13009/EUCASS2017-247

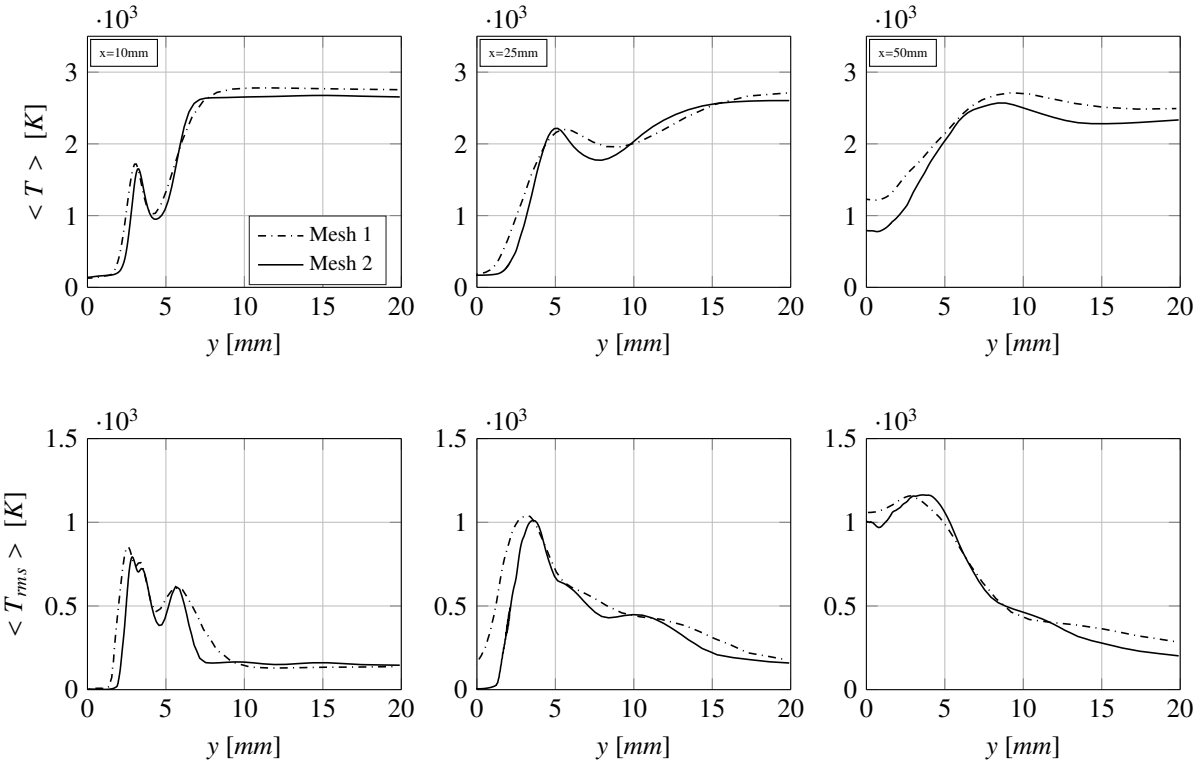

Figure 7: Mesh sensitivity analysis at $x/h = 10$.

which is a conservative assessment since acceleration due to combustion is not included. Then the flow through time T_{ft} is calculated using the length of the window of 100 mm by

$$T_{ft} = \frac{100\,\text{mm}}{U_{conv}} \approx 2.5\,\text{ms}. \tag{13}$$

Consequently, a simulation has been run for $2 \cdot T_{ft}$, $5 \cdot T_{ft}$ and $10 \cdot T_{ft}$ to justify the estimation. Fig. 8 shows the time-averaged density and its time-averaged RMS values along the centerline for the three averaging intervals. Obviously the first moments converge rather fast and almost no differences can be observed between $5 \cdot T_{ft}$ and $10 \cdot T_{ft}$. The second moments take longer to converge, especially in regions of high fluctuations. Based on this evaluation, statistics are collected for $5 \cdot T_{ft}$ in the five-element injector simulation.

Sensitivity to turbulent inlet boundary conditions

A sensitivity analysis is conducted in order to quantify the impact of the turbulence inlet boundary conditions. Two simulations are run on the medium mesh using a statistically converged flow field as initial condition. In the first

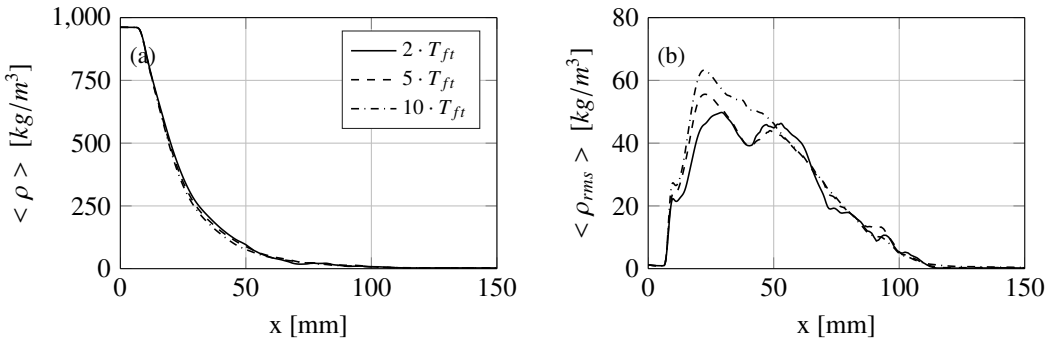

Figure 8: Analysis of time averaging requirements: Time-averaged density and its RMS along the axis for three averaging intervals.

DOI: 10.13009/EUCASS2017-247

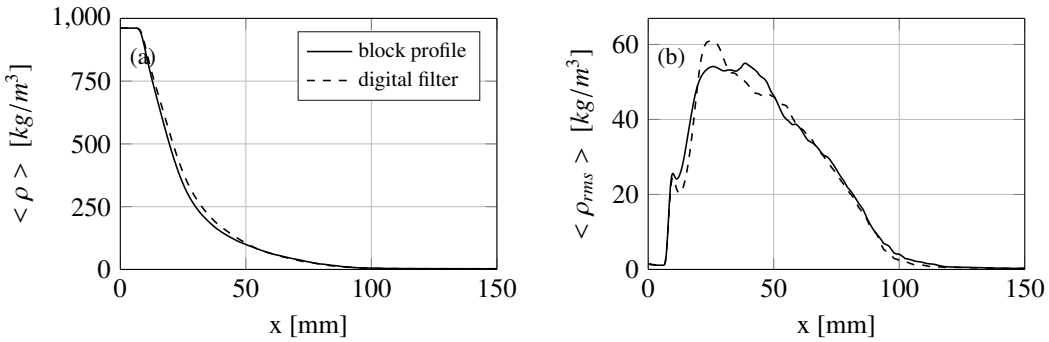

Figure 9: Effect of turbulent inlet boundary conditions: Time-averaged density and its RMS along the axis.

simulation, the inlet velocity is prescribed as a block-profile without fluctuations using the mean value given by the experimental data. For the second simulation, turbulent inlet boundary conditions are generated using the digital filter method by Klein *et. al.*,[11] which has been implemented to OpenFOAM by Immer.[10] A hyperbolic tangent function is used as mean velocity profile for both the oxidizer pipe and the fuel annulus in the second case. Consequently, both simulations are run for $10 \cdot T_{ft}$ to collect the statistics. Fig. 9 shows the first and second moments of the density along the axis of the domain. The results emphasize that in this case the turbulence inlet boundary conditions have only minor effect on the mean flow field since turbulence is mostly produced in the shear layer between the propellants. Only slight differences can be observed between $x = 25$ mm to $x = 50$ mm. Hence turbulent fluctuations at the inlet are neglected for the full injector simulation.

4.2 Full Injector Configuration

Instantaneous flow field

A qualitative impression of the flame structure is given in Fig. 10. The snapshots represent a diagonal cut through the domain, such that the flow emanating from three aligned injection elements is captured. The instantaneous temperature field shows a highly wrinkled flame surface caused by the resolved turbulence. Due to the large injection velocity difference of $u_{H_2,in} = 410\,\mathrm{m\,s^{-1}}$ and $u_{O_2,in} = 12.3\,\mathrm{m\,s^{-1}}$, the shear layer experiences strong shear forces and shows the typical instabilities and finger-like structures. It can bee seen that the outer flames are slightly deflected, while the central core remains mostly axially, which has been experimentally observed.[7] The instantaneous O_2 field shows an intact central LOx core up to $x \approx 55$ mm, where hot gas pockets begin to deform it. Further downstream, large structures of oxygen break away from the core. The magnitude of the density gradient emphasizes the structure of the three cold cores. Additionally, the OH^* emission is computed to highlight the reaction zone according to Fiala and Sattelmayer[4] as

$$c_{OH^*} = c_{OH} \cdot exp\left(-\frac{hc}{k_B \lambda T}\right), \tag{14}$$

where h is the Planck constant, c the speed of light, k_B the Boltzmann constant and $\lambda = 308$ nm. OH^* emission is observed in the shear layer directly downstream of the injection elements with increasing intensity as the flames start to interact. Maximum reaction activity in this instantaneous diagonal cut takes place starting from $x \approx 50$ mm, in the region where the outer flames mix with the central one.

Interaction between injector elements

The injector footprint and the mixing process is visualized using cuts of the temperature field in Fig. 11 and the mixture fraction in Fig. 12 at five axial positions. In both figures, the top half shows an instantaneous snapshot and the bottom half shows the respective time-averaged field. At the first position, $x = 10$ mm, the flames are still very thin and the concentric shape is clearly determined by the injector elements. Further downstream at $x = 25$ mm, hot gas pockets can instantaneously be observed between the flames while the mean fields still show visible separation. Starting from $x = 50$ mm, the flames mix and form a very hot zone in the region of interaction, although the cold LOx core still persists. Downstream of $x = 100$ mm the flow field is fully mixed and the interaction with the H_2 co-flow and the H_2 cooling film becomes dominant. While the coolant film remains intact up to $x = 50$ mm, one can observe that large turbulent structures penetrate the film further downstream leading to mutual transport of hot and cold gas and thereby

DOI: 10.13009/EUCASS2017-247

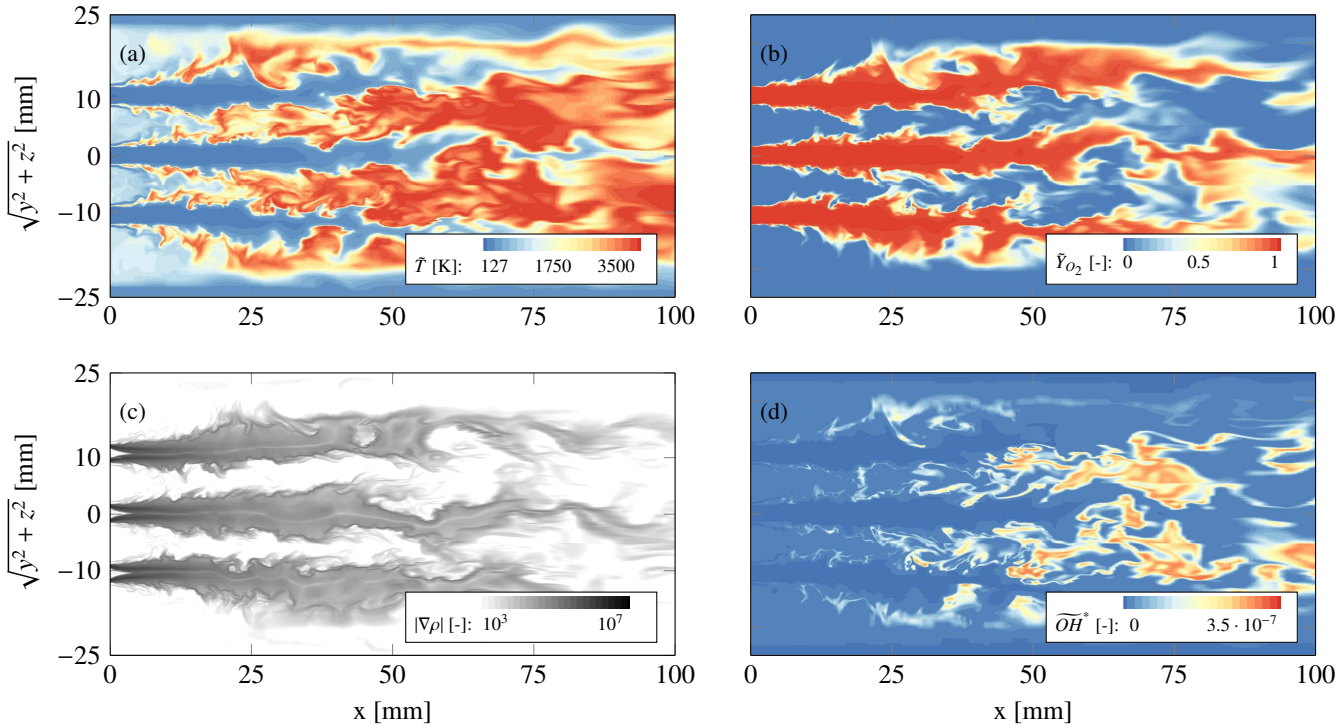

Figure 10: Diagonal cut in the instantaneous flow field of the multi element simulation.

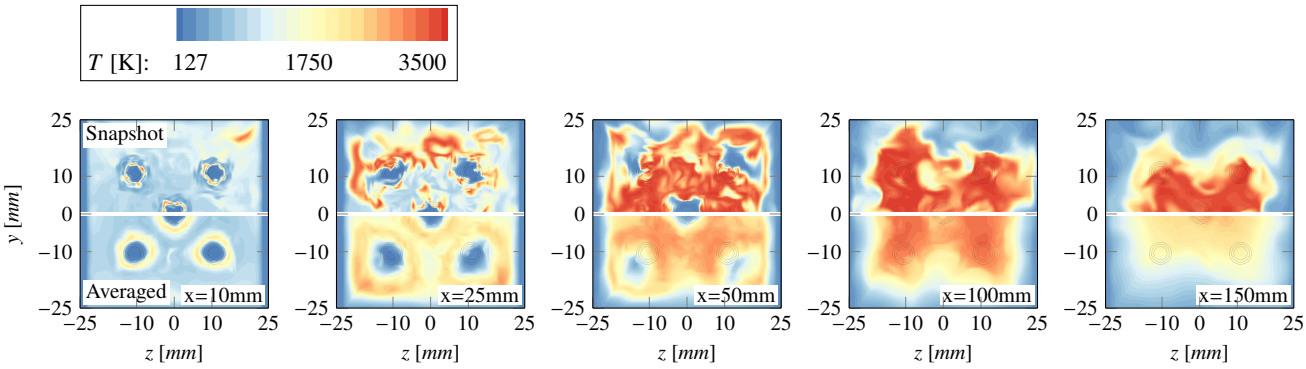

Figure 11: Axial evolution of the injector footprint in terms of temperature distribution.

form a growing layer with moderate temperatures in the time-averaged field. This mixing continues and at $x = 150$ mm the mean hot gas temperature is clearly reduced due to mixing with the cooling film in the whole cross-section. Figs. 11 and 12 additionally show that the central flame remains axially while the outer flames are radially deflected towards cooling film and co-flow. Directly downstream of the faceplate, the cold cores are still aligned with the coaxial shear element which is already not the case at $x = 25$ mm becomes more evident further downstream.

Comparison with experimental data

As a first approach to compare the LES results with the experimental data, 30 equidistant slices normal to the y-x-plane are selected and the mean value of the numerical data is calculated. This is a preliminary procedure as the statistics are not exactly captured in that manner. However, it allows for a qualitative comparison with the experimental instantaneous and time-averaged shadowgraphy and OH* emission images. In Fig. 13, the time-averaged experimental results are obtained from 2400 frames for OH* and 700 frames for the shadowgraph picture, respectively. Numerically, the shadowgraphy image is approximated by the magnitude of the second derivative of the density.[29] The OH* radiation is expressed by the method of Fiala and Sattelmayer.[4] The shadowgraphy images allow for a qualitative evaluation of the dense LOx structures and the regions of high density gradients. The predicted general flame structure is in agreement with the experimental results. One can identify the cold oxygen cores with the shedding of large structures

DOI: 10.13009/EUCASS2017-247

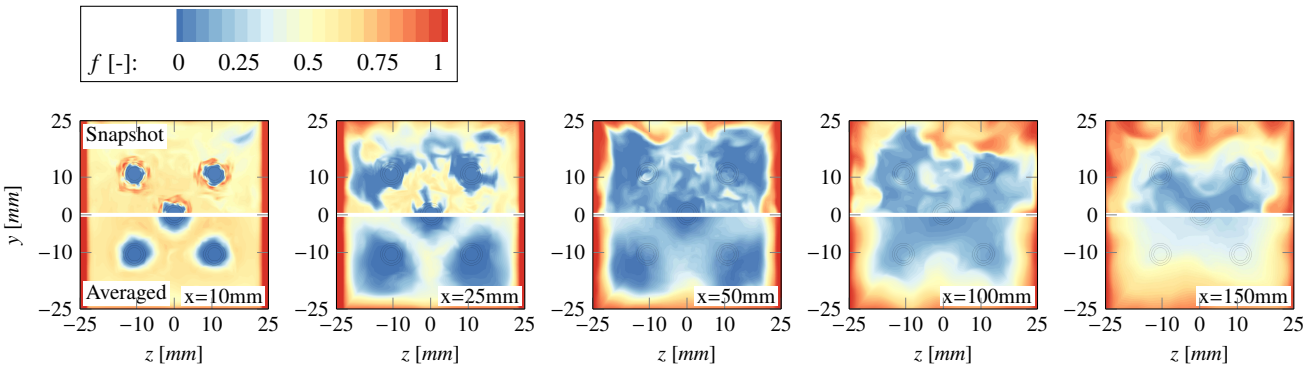

Figure 12: Axial evolution of the mixture fraction.

as well as the interaction between the flames. However, the time-averaged results indicate that the core length is underpredicted by the LES, which could be related to insufficient mesh resolution, as shown in Fig. 7. The interpretation of OH* emission is difficult as the lateral averaging represents only a rudimentary approach to reproduce the experimental line-of-sight image. In both experiment and simulation the major reaction intensity is located in the second half of the window region. In the instantaneous snapshots suggest that the OH* intensity towards the faceplate is lower in the simulation. Moreover, strong OH* radiation can be observed in the region where the flames interact while only few signals are detected on the flame sides towards the co-flow. At this point, the comparison between experiment and simulation is purely qualitative and further data processing of the LES results is ongoing. Possible improvements in terms of OH* emission could be obtained by solving a transport equation for OH radiation in optically thick gases.

5. Conclusion

A method to reduce the computational cost of incorporating real-gas thermodynamics into LES of non-premixed combustion at supercritical pressures is presented. According to the steady laminar flamelet approach the chemical reactions are assumed to be fast compared to the turbulent time scales, which is sensible at the considered operating conditions. The formulation uses the species mass fractions of one-dimensional ideal gas counter-flow diffusion flames and consequently computes the real-gas thermodynamics based on the Peng-Robinson equation of state for the particular mixture. The use of an accurate equation of state, the correction of the enthalpy with its pressure-dependent part and the application of a suitable transport model allows for a precise representation of the thermo-chemical state. A β-shaped PDF is employed to model SGS fluctuations. By the resulting formulation, the real-gas calculations can be outsourced to a pre-processing step and the computational cost of the simulations are comparable to ideal gas computations.

LES of the five-element LOx/H$_2$ rocket combustor BKH operated at DLR Lampoldshausen by Hardi *et al.*[7,8] are carried out to exploit the applicability of the proposed method. Instantaneous and time-averaged flow features are examined and the interaction between the injection elements is investigated. The numerical results are compared to experimental shadowgraphy and OH* emission images. The analysis shows that the general flame structure agrees with the experiment, despite differences especially in the time-averaged oxygen core length could be observed. First comparisons of OH* emissions emphasize that the main reaction zone is well captured although a better method is required to evaluate the line-of-sight experimental images within the numerical data.

6. Acknowledgments

The authors gratefully acknowledge the German Research Foundation (Deutsche Forschungsgemeinschaft) for providing financial support in the framework of SFB/TR 40 *Fundamental Technologies for the Development of Future Space-Transport-System Components under High Thermal and Mechanical Loads* and the Gauss Centre for Supercomputing e.V. (www.gauss-centre.eu) for funding this project by providing computing time on the GCS Supercomputer SuperMUC at Leibniz Supercomputing Centre (LRZ, http://www.lrz.de).

References

[1] B. Chehroudi. Recent experimental efforts on high-pressure supercritical injection for liquid rockets and their implications. *International Journal of Aerospace Engineering*, 2012, 2012.

DOI: 10.13009/EUCASS2017-247

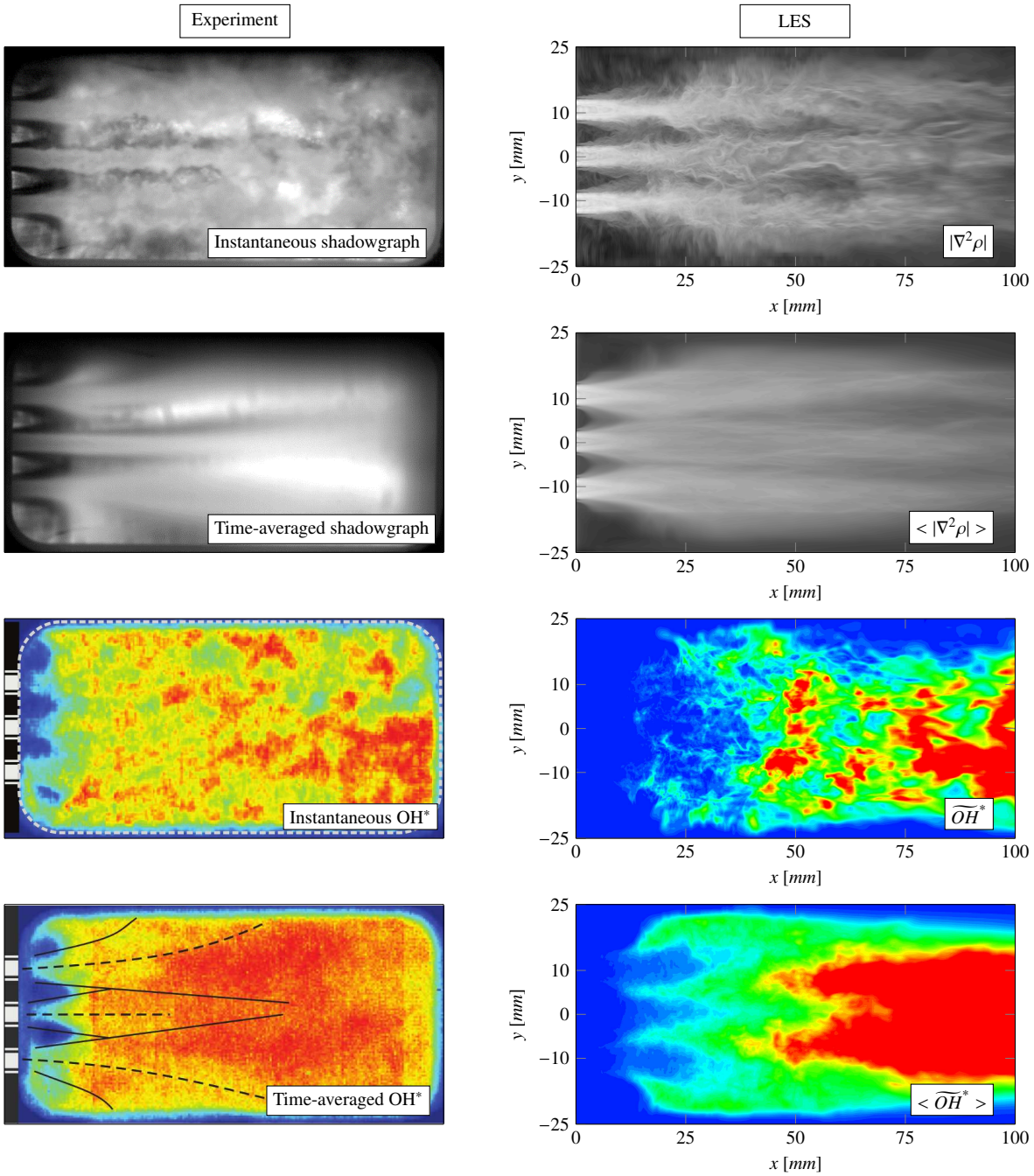

Figure 13: Comparison with experimental data: First row shows instantaneous shadowgraphy image and a snapshot of the magnitude of the second derivative of the density. Second row depicts the respective time averaged quantities. Third and fourth row show instantaneous and time-averaged OH* emissions.

DOI: 10.13009/EUCASS2017-247

[2] T.-H. Chung, M Ajlan, L L Lee, and K E Starling. Generalized multiparameter correlation for nonpolar and polar fluid transport properties. *Industrial & Engineering Chemistry Research*, 27(4):671–679, 1988.

[3] A.W. Cook and W.H. Cabot. Hyperviscosity for shock-turbulence interactions. *Journal of Computational Physics*, 203(3):2133–2144, 2005.

[4] T. Fiala and T. Sattelmayer. Assessment of existing and new modeling strategies for the simulation of OH* radiation in high-temperature flames. *CEAS Space Journal*, 8(1):47–58, 2016.

[5] N. Guezennec, M. Masquelet, and S. Menon. Large Eddy Simulation of flame-turbulence interactions in a LOX-CH4 shear coaxial injector. In *50th AIAA Aerospace Sciences Meeting including the New Horizons Forum and Aerospace Exposition: AIAA paper 2012-1267*, 2012.

[6] L. Hakim, A. Ruiz, T. Schmitt, M. Boileau, G. Staffelbach, B. Cuenot, and S. Candel. Large eddy simulations of multiple transcritical coaxial flames submitted to a high-frequency transverse acoustic modulation. *Proceedings of the Combustion Institute*, 35(2):1461–1468, 2015.

[7] J. S. Hardi, S. Beinke, M. Oschwald, and B. B. Dally. Coupling of Cryogenic Oxygen-Hydrogen Flames to Longitudinal and Transverse Acoustic Instabilities. *Journal of Propulsion and Power*, 30(4):991–1004, 2014.

[8] J. S. Hardi, H. C. Gomez Martinez, M. Oschwald, and B. B. Dally. LOx Jet Atomization Under Transverse Acoustic Oscillations. *Journal of Propulsion and Power*, 30(2):337–349, 2014.

[9] K. G. Harstad, R. S. Miller, and J. Bellan. Efficient high-pressure state equations. *AIChE Journal*, 43(6):1605–1610, 1997.

[10] M.C. Immer. *Time-resolved measurement and simulation of local scale turbulent urban flow*. PhD thesis, ETH Zürich, 2016.

[11] M. Klein, A. Sadiki, and J. Janicka. A digital filter based generation of inflow data for spatially developing direct numerical or large eddy simulations. *Journal of Computational Physics*, 186(2):652–665, 2003.

[12] G. Lacaze and J. C. Oefelein. A non-premixed combustion model based on flame structure analysis at supercritical pressures. *Combustion and Flame*, 159(6):2087–2103, 2012.

[13] P.J. Linstrom and W.G. Mallard, editors. *NIST Chemistry WebBook NIST Standard Reference Database Number 69*. National Institute of Standards and Technology, Gaithersburg, 2017.

[14] H. Mayer, W.and Tamura. Propellant injection in a liquid oxygen/gaseous hydrogen rocket engine. *Journal of Propulsion and Power*, 12(6):1137–1147, 1996.

[15] W. Mayer, A. Schik, B. Vielle, C. Chaveau, I. Gökalp, and D. Talley. Atomization and breakup of cryogenic propellants under high pressure subcritical and supercritical conditions. *Journal of Propulsion and Power*, 14(5):835–842, 1998.

[16] H. Müller, C.A. Niedermeier, J. Matheis, M. Pfitzner, and S. Hickel. Large-eddy simulation of nitrogen injection at trans- and supercritical conditions. *Physics of Fluids*, 28:015102, 2016.

[17] H. Müller and M. Pfitzner. Large-eddy simulation of transcritical LOx/CH4 jet flames. *6^{th} European Conference for Aeronautics and Space Sciences (EUCASS)*, June 2015.

[18] H. Müller, M. Pfitzner, J. Matheis, and S. Hickel. Large-Eddy Simulation of Coaxial LN2/GH2 Injection at Trans- and Supercritical Conditions. *Journal of Propulsion and Power*, 32(1):46–56, 2015.

[19] M. O'Connaire, H.J. Curran, J.M. Simmie, W.J. Pitz, and C.K. Westbrook. A comprehensive modeling study of hydrogen oxidation. *International Journal of Chemical Kinetics*, 36:603–622, 2004.

[20] J. Oefelein and V. Yang. Modeling high-pressure mixing and combustion processes in liquid rocket engines. *Journal of Propulsion and Power*, 14(5):843–857, 1998.

[21] J. C. Oefelein. Thermophysical characteristics of shear-coaxial LOX-H2 flames at supercritical pressure. *Proceedings of the Combustion Institute*, 30:2929–2937, 2005.

[22] M. Oschwald, J. J. Smith, R. Branam, J. Hussong, A. Schik, B. Chehroudi, and D. Talley. Injection of fluids into supercritical environments. *Combustion Science and Technology*, 178(1-3):49–100, 2006.

DOI: 10.13009/EUCASS2017-247

[23] D.-Y. Peng and D. B. Robinson. A new two-constant equation of state. *Industrial & Engineering Chemistry Fundamentals*, 15(1):59–64, 1976.

[24] N. Peters. *Turbulent combustion*. Cambridge University Press, 2000.

[25] B. E. Poling, J. M. Prausnitz, and J. P. O'Connell. *The properties of gases and liquids*. Mc Graw Hill, 2001.

[26] G. Ribert, N. Zong, V. Yang, L. Pons, N. Darabiha, and S. Candel. Counterflow diffusion flames of general fluids: Oxygen/hydrogen mixtures. *Combustion and Flame*, 154(3):319–330, 2008.

[27] A.M. Ruiz, G. Lacaze, J.C. Oefelein, R. Mari, B. Cuenot, L. Selle, and T. Poinsot. Numerical Benchmark for High-Reynolds-Number Supercritical Flows with Large Density Gradients. *AIAA Journal*, 54(5):1445–1460, 2016.

[28] T. Schmitt, Y. Méry, M. Boileau, and S. Candel. Large-Eddy Simulation of oxygen/methane flames under transcritical conditions. *Proceedings of the Combustion Institute*, 33:1383–1390, 2011.

[29] G.S. Settles. *Schlieren and Shadowgraph Techniques*. Springer, Berlin, 1st edition, 2001.

[30] G.G. Simeoni, T. Bryk, F.A. Gorelli, M. Krisch, G. Ruocco, M. Santoro, and T. Scopigno. The Widom line as the crossover between liquid-like and gas-like behaviour in supercritical fluids. *Nature Physics*, 6:503–507, 2010.

[31] H. Terashima, S. Kawai, and N. Yamanishi. High-resolution numerical method for supercritical flows with large density variations. *AIAA Journal*, 49(12):2658–2672, 2011.

[32] A. Urbano, L. Selle, G. Staffelbach, B. Cuenot, T. Schmitt, S. Ducruix, and S. Candel. Exploration of combustion instability triggering using Large Eddy Simulation of a multiple injector liquid rocket engine. *Combustion & Flame*, 169:129–140, 2016.

[33] A.W. Vreman. An eddy-viscosity subgrid-scale model for turbulent shear flow: Algebraic theory and applications. *Physics of Fluids*, 16(10):3670–3681, 2004.

[34] N. Zong, H. Meng, S. Y. Hsieh, and V. Yang. A numerical study of cryogenic fluid injection and mixing under supercritical conditions. *Physics of Fluids (1994-present)*, 16(12):4248–4261, 2004.